Los Alamos NATIONAL LABORATORY EST.1943

LA-UR-18-26786 (Accepted Manuscript)

Large-scale Compression Acceleration during Magnetic Reconnection in a Low-ß Plasma

Li, Xiaocan
Guo, Fan
Li, Hui
Li, Shengtai

Provided by the author(s) and the Los Alamos National Laboratory (2018-12-17).

To be published in: The Astrophysical Journal

DOI to publisher's version: 10.3847/1538-4357/aae07b

Permalink to record: http://permalink.lanl.gov/object/view?what=info:lanl-repo/lareport/LA-UR-18-26786

Disclaimer:
Approved for public release. Los Alamos National Laboratory, an affirmative action/equal opportunity employer, is operated by the Los Alamos National Security, LLC for the National Nuclear Security Administration of the U.S. Department of Energy under contract DE-AC52-06NA25396. Los Alamos National Laboratory strongly supports academic freedom and a researcher's right to publish; as an institution, however, the Laboratory does not endorse the viewpoint of a publication or guarantee its technical correctness.

RESEARCH LIBRARY

The Astrophysical Journal, 866:4 (12pp), 2018 October 10 https://doi.org/10.3847/1538-4357/aae07b
© 2018. The American Astronomical Society.
OPEN ACCESS

Large-scale Compression Acceleration during Magnetic Reconnection in a Low-β Plasma

Xiaocan Li[1], Fan Guo[1,2], Hui Li[1], and Shengtai Li[1]
[1] Los Alamos National Laboratory, Los Alamos, NM 87545, USA; xiaocanli@lanl.gov
[2] New Mexico Consortium, Los Alamos, NM 87544, USA
Received 2018 July 9; revised 2018 August 28; accepted 2018 September 6; published 2018 October 5

Abstract

In solar flares and other astrophysical systems, a major challenge for solving the particle acceleration problem associated with magnetic reconnection is the enormous scale separation between kinetic scales and the observed reconnection scale. Because of this, it has been difficult to draw any definite conclusions by just using kinetic simulations. A particle acceleration model that solves the energetic particle transport equation can capture the main acceleration physics found in kinetic simulations and thus provide a practical way to make observable predictions and directly compare model results with observations. Here we study compression particle acceleration in magnetic reconnection by solving the Parker (diffusion–advection) transport equation using velocity and magnetic fields from two-dimensional magnetohydrodynamics (MHD) simulations of a low-β high-Lundquist-number reconnection layer. We show that the compressible reconnection layer can give significant particle acceleration, leading to the formation of power-law particle energy distributions. We analyze the acceleration rate and find that the acceleration in the reconnection layer is a mixture of first- and second-order Fermi processes. When including a guide field, we find that the spectrum becomes steeper and both the power-law cutoff energy and maximum particle energy decrease as plasma becomes less compressible. This model produces a 2D particle distribution that one can use to generate a radiation map and directly compare with solar flare observations. This provides a framework to explain particle acceleration at large-scale astrophysical reconnection sites, such as solar flares.

Key words: acceleration of particles – magnetic reconnection – Sun: corona – Sun: flares

1. Introduction

Energy conversion and particle acceleration in strongly magnetized plasmas are important processes that hold the key for understanding many explosive solar and astrophysical high-energy phenomena (Zweibel & Yamada 2009; Lin 2011). Magnetic reconnection is a major mechanism that drives the release of magnetic energy and nonthermal particle acceleration by reorganizing the topology and connectivity of magnetic field lines (Fu et al. 2013a, 2017). One of the best examples of magnetic reconnection and the associated particle acceleration is solar flares. Observations have suggested that magnetic reconnection converts 10%–50% of the magnetic energy (up to $\sim 10^{33}$ erg) into plasma kinetic energy within 1–10 minutes. During the process, a large amount of electrons in the flare region ($>10^{36}$ electrons) are accelerated into a power-law energy spectrum $f(\varepsilon) \propto \varepsilon^{-s}$ with a spectral index from $s \sim 3$ to more than $s = 9$ with a median of about 5 (Lin & Hudson 1976; Krucker et al. 2010; Oka et al. 2013, 2015; Effenberger et al. 2017). The acceleration of ions in a flare region can be as efficient as that of electrons. This is suggested by *RHESSI*'s observation of the correlation between electron-generated hard X-ray flux and ion-generated γ-ray flux (Shih et al. 2009). In situ solar energetic particle (SEP) observation has also shown that the electron and ion spectra often resemble power-law distributions (Mason et al. 2012). How such efficient particle acceleration occurs over a large-scale reconnection region remains an important unsolved problem in reconnection study.

Original content from this work may be used under the terms of the Creative Commons Attribution 3.0 licence. Any further distribution of this work must maintain attribution to the author(s) and the title of the work, journal citation and DOI.

During solar flares, large-scale magnetic reconnection is in the weakly collisional (high Lundquist number) regime and is likely to have magnetic structures with a range of spatial scales. One attractive scenario that emerged in the past decade is the plasmoid-dominated reconnection, where a hierarchy of plasmoids develop in a macroscopic reconnection layer (Shibata & Tanuma 2001; Loureiro et al. 2007; Bhattacharjee et al. 2009; Comisso et al. 2016) and naturally bring the current sheet from the macroscopic scale to the kinetic scale (Daughton et al. 2009; Ji & Daughton 2011). It is therefore important to study particle acceleration in magnetic reconnection using a multiscale approach. For magnetic reconnection at kinetic scales, kinetic simulations provide a first-principle description of particle acceleration, but the domain size is limited due to the demanding computational expense. The standard approach to study particle acceleration on large scales is to solve the energetic particle transport equation (e.g., Parker 1965; Zank et al. 2014), but this has not been applied in reconnection study until recently (see below for a more detailed discussion). Instead, test-particle simulations have been widely used to study particle acceleration during reconnection on large scales. Below, we review the previous theories and numerical simulations on particle acceleration in magnetic reconnection.

Particle-in-cell (PIC) kinetic simulation has been popular in modeling particle acceleration during magnetic reconnection, as it includes the full range of plasma physics. Previous kinetic simulations have extensively studied several acceleration mechanisms, such as direct acceleration close to the reconnection X-point (Hoshino et al. 2001; Drake et al. 2005; Fu et al. 2006; Oka et al. 2010; Egedal et al. 2012, 2015; Wang et al. 2016), Fermi-type acceleration in contracting magnetic islands (Drake et al. 2006; Oka et al. 2010), acceleration in island-merging regions (Oka et al. 2010; Liu et al. 2011;

Drake et al. 2013; Nalewajko et al. 2015), and acceleration at the reconnection front (Fu et al. 2011, 2012; Liu et al. 2017a, 2017b; Xu et al. 2018). By summing over the particle guiding-center motions, several recent studies have identified curvature drift along the motional electric field as the major particle acceleration mechanism (Dahlin et al. 2014; Guo et al. 2014, 2015; Li et al. 2015, 2017) in the weak guide-field case. However, because of the enormous scale separation between kinetic scales (ion skin depth ~10–100 m) and the scale of the observed reconnection region ($\sim 10^7$ m), it has been difficult to draw any definite conclusion and compare solar flare observations with the modeling results. To overcome this major difficulty and solve the particle acceleration problem in solar flare reconnection, one has to come up with a description for the acceleration of particles at a macroscopic fluid scale.

Test-particle simulations are widely used in studying particle acceleration during solar flares. Both full particle orbits and particle guiding-center motions have been calculated in background electric and magnetic fields provided by MHD simulations. Under the guiding-center approximation, one can solve particle motions in realistic scales by removing the high-frequency gyromotions. The test-particle method usually generates hard power-law energy spectra (Onofri et al. 2006; Gordovskyy et al. 2010a, 2010b; Zhou et al. 2015, 2016) that can extend to tens of keV for electrons and tens of MeV for protons but may be too hard to explain the observations (power-law index for electrons $1 < s < 2$). Acceleration due to the parallel electric field is usually the dominant particle acceleration mechanism found in the these simulations. This is likely due to the large anomalous resistivity and coarse grids used in these simulations, resulting in much broader current layers and a much larger resistive electric field than that in real systems. Furthermore, the large anomalous resistivity is not supported by current 3D PIC simulations of reconnection layers (Roytershteyn et al. 2012; Liu et al. 2013; Le et al. 2018). One can avoid this problem by ignoring the parallel electric field completely (Zhou et al. 2015; Birn et al. 2017), leading to particle energy spectra that are close to solar flare observations. But this method still does not take into account the effect of wave–particle interaction that scatters particles and changes the acceleration processes.

The standard approach to solve the large-scale particle acceleration and transport problem is to use the energetic particle transport theory, which has been widely used in studying shock acceleration and cosmic-ray transport. The primary acceleration mechanism is due to adiabatic compression and is included in the Parker transport equation (Parker 1965; Blandford & Eichler 1987). Various other acceleration mechanisms (e.g., fluid shear and fluid acceleration) could also be included in the transport theory (Earl et al. 1988; Zank 2014). It is worth noting that the acceleration due to curvature and gradient drift that was found to be important in earlier kinetic simulations has also been included in the transport theory (Jones 1990; le Roux & Webb 2009). Several studies have attempted to develop similar transport theories (or reduced kinetic equations) for studying particle acceleration during reconnection (Drake et al. 2006, 2013; Egedal et al. 2013; Zank 2014; le Roux et al. 2015; Montag et al. 2017). These studies include previously studied particle acceleration mechanisms, such as the parallel reconnection electric field and contracting and merging magnetic islands. While some of the studies assume that the reconnection layer is incompressible and only consider incompressible effects (e.g., Drake et al. 2006, 2013), other recent studies emphasized both compressible and incompressible effects (Zank et al. 2014; le Roux et al. 2015; Montag et al. 2017). Recently, for the first time, Li et al. (2018) used fully kinetic simulations to show that compression energization dominates the acceleration of high-energy particles in reconnection with a weak guide field (<20% of the reconnecting component), and the compression and shear effects are comparable when the guide field is moderate (~0.5 times the reconnecting magnetic field component). Meanwhile, some recent MHD simulations also suggest that the reconnection layer is compressible, especially when the plasma β is low and the guide field is weak (Birn et al. 2012; Provornikova et al. 2016). These simulation results suggest that one may study particle acceleration in a large-scale solar flare reconnection site using the transport theory.

Drury (2012) considered reconnection acceleration by assuming the reconnection region as a black box with a certain compression ratio r between the upstream and downstream regions. He found that compression acceleration leads to a power-law spectrum $f(p) \propto p^{-\chi}$ and the spectral index depends on the compression ratio in a similar way as in diffusive shock acceleration $\chi = -3r/(r-1)$. For nonrelativistic particles, the spectral index s for energy spectrum $f(\varepsilon)$ is related to χ by $s = (\chi - 1)/2$. As discussed above, the reconnection layer in the weakly collisional regime may have magnetic structures in various scales. It is worthwhile to study whether the power-law energy spectrum can still develop and how the spectral features depend on the key plasma parameters of the reconnection layer. The goal of this paper is to study large-scale compression acceleration during magnetic reconnection in the plasmoid-dominated regime.

In this paper, we solve the Parker (diffusion–advection) transport equation using the background velocity and magnetic fields from MHD simulations of a low-β high-Lundquist-number reconnection layer. We assume that electrons and protons are already energetic and can interact with the background magnetic fluctuation in the reconnection region. In Section 2, we describe the MHD simulations and stochastic integration method for solving the Parker transport equation. In Section 3, we present our simulation results. We show that particles are significantly accelerated by the compression reconnection layer in the plasmoid-dominated regime. The acceleration leads to the formation of a power-law energy distribution for both electrons and protons. The power-law index, cutoff energy, and maximum energy depend on the guide-field strength and the diffusion model. This model also produces a 2D particle distribution that one can use to generate a radiation map and directly compare with observations. This provides a framework to explain particle acceleration at large-scale reconnection sites, such as solar flares. In Section 4, we discuss the conclusions and implications based on our simulation results.

2. Numerical Methods

2.1. MHD Simulations

We carry out simulations of magnetic reconnection using the Athena MHD code (Stone et al. 2008). We use a third-order piecewise parabolic reconstruction, the Harten–Lax–van Leer discontinuities Riemann solver, the MUSCL-Hancock (VL) integrator, and the constrained transport (CT) algorithm to

ensure the divergence-free state of the magnetic field. The code solves the resistive MHD equations

$$\frac{\partial \rho}{\partial t} + \nabla \cdot (\rho \boldsymbol{v}) = 0,$$
$$\frac{\partial (\rho \boldsymbol{v})}{\partial t} + \nabla \cdot \left[\rho \boldsymbol{v}\boldsymbol{v} + \left(p + \frac{\boldsymbol{B}\cdot\boldsymbol{B}}{2}\right)\boldsymbol{I} - \boldsymbol{B}\boldsymbol{B}\right] = 0,$$
$$\frac{\partial e}{\partial t} + \nabla \cdot \left[\left(e + p + \frac{\boldsymbol{B}\cdot\boldsymbol{B}}{2}\right)\boldsymbol{v} - \boldsymbol{B}(\boldsymbol{B}\cdot\boldsymbol{v})\right] = \nabla \cdot (\boldsymbol{B} \times \eta \boldsymbol{j}),$$
$$\frac{\partial \boldsymbol{B}}{\partial t} - \nabla \times (\boldsymbol{v} \times \boldsymbol{B}) = \eta \nabla^2 \boldsymbol{B},$$

where

$$e = \frac{p}{\gamma - 1} + \frac{\rho \boldsymbol{v}\cdot\boldsymbol{v}}{2} + \frac{\boldsymbol{B}\cdot\boldsymbol{B}}{2}, \quad \boldsymbol{j} = \nabla \times \boldsymbol{B},$$

where ρ is the mass density, $\boldsymbol{v}$ is the velocity, e is the total energy density, $\boldsymbol{B}$ is the magnetic field, p is the gas pressure, γ (=5/3) is the adiabatic index, $\boldsymbol{j}$ is the current density, and η is the resistivity. Unless specified otherwise, we normalize the simulations by $L_0 = 5000$ km (the simulation box size is 10^4 km) and $v_A = 1000\,\mathrm{km\,s^{-1}}$, which are the typical parameters of the reconnection site of a solar flare. We assume the normalized magnetic field $B_0 = 50$ G and the particle density is $1.2 \times 10^{10}\,\mathrm{cm^{-3}}$. We choose $\eta = 10^{-5}$ and the same box sizes $L_x = L_y = 2$ in all simulations, resulting in a Lundquist number $S = L_y v_A/(2\eta) = 10^5$. The simulation box is $x \in [0, 2]$ and $y \in [0, 2]$. The simulations start from two current sheets with

$$\boldsymbol{B} = B_0\left[\tanh\left(\frac{x - x_1}{\lambda}\right) - \tanh\left(\frac{x - x_2}{\lambda}\right)\right]\hat{y} - B_0\hat{y} + B_0\left[\sqrt{\mathrm{sech}^2\left(\frac{x - x_1}{\lambda}\right) + \frac{B_g^2}{B_0^2}} + \sqrt{\mathrm{sech}^2\left(\frac{x - x_2}{\lambda}\right) + \frac{B_g^2}{B_0^2}} - \frac{B_g}{B_0}\right]\hat{z}, \quad (1)$$

where $B_0 = 1.0$ is the strength of the reconnecting magnetic field, B_g is the strength of the guide field, $x_1 = 0.5$ and $x_2 = 1.5$ are the x-positions of the current sheets, and $\lambda = 0.005$ is the half thickness of the current sheet. The grid sizes are $n_x \times n_y = 8192 \times 4096$, so we can resolve the initial current sheet by at least 10 cells. We employ an initial magnetic flux perturbation to speed up the reconnection onset,

$$\psi_z(x, y) = \psi_0 B_0\left[\cos\left(\frac{2\pi(x - x_1)}{L_x}\right) - \cos\left(\frac{2\pi(x - x_2)}{L_x}\right)\right]\cos\left(\frac{2\pi y}{L_y}\right), \quad (2)$$

where ψ_0 is the amplitude of the perturbation. Initially, the total pressure (gas pressure + magnetic pressure) is uniform in the simulation box. We choose $\psi_0 = 10^{-4}$ so that the initial density variation is under 2.6%. The initial plasma $\beta = 2p/B^2 \approx 0.1$. We choose periodic boundary conditions along both the x and y directions. We perform four simulations with $B_g = 0$, 0.2, 0.5, and 1.0. The initial plasma density $\rho_0 \approx 1.0, \sqrt{1.04}, \sqrt{1.25}$, and $\sqrt{2}$, so the resulting Alfvén speed $v_A = \sqrt{(B_0^2 + B_g^2)/\rho_0}$ in the reconnection inflow region ≈ 1.0 for all four runs. Note that the Lundquist number in the simulations is much smaller than the realistic number calculated from the Coulomb collision. Previous numerical simulations have shown that the reconnection rate becomes a few percent of the Alfvén speed and independent of the Lundquist number when $S \gtrsim 10^4$ (e.g., Bhattacharjee et al. 2009; Huang & Bhattacharjee 2010).

2.2. Solving the Parker Transport Equation

We then solve Parker's transport equation,

$$\frac{\partial f}{\partial t} + (\boldsymbol{v} + \boldsymbol{v}_d)\cdot\nabla f - \frac{1}{3}\nabla\cdot\boldsymbol{v}\frac{\partial f}{\partial \ln p} = \nabla\cdot(\boldsymbol{\kappa}\nabla f) + Q, \quad (3)$$

where $f(x_i, p, t)$ is the particle distribution function as a function of the particle position x_i, momentum p (isotropic momentum assumed), and time t; $\boldsymbol{\kappa}$ is the spatial diffusion coefficient tensor, $\boldsymbol{v}$ is the bulk plasma velocity, and Q is the source. Note that the particle drift $\boldsymbol{v}_d$ is out of the simulation plane and is not considered here. We assume an isotropic particle distribution here based on earlier results of kinetic simulations (Li et al. 2018), where we showed that the anisotropy is weak for high-energy electrons and becomes even weaker as the simulation evolves. This indicates that plasma waves (or turbulence in 3D) can scatter particles to isotropize the particle distribution. The diffusion coefficient tensor is given by

$$\kappa_{ij} = \kappa_\perp \delta_{ij} - \frac{(\kappa_\perp - \kappa_\parallel)B_i B_j}{B^2}, \quad (4)$$

where $\kappa_\parallel$ and $\kappa_\perp$ are the parallel and perpendicular diffusion coefficients. Here $\kappa_\parallel$ can be calculated from the quasi-linear theory (Jokipii 1971). Assuming that magnetic turbulence is well developed and has an isotropic power spectrum $P \sim k^{-5/3}$, the resulting $\kappa_\parallel \sim p^{4/3}$ when the particle gyroradius is much smaller than the correlation length of turbulence. In particular, we use the following expression for $\kappa_\parallel$ (Giacalone & Jokipii 1999),

$$\kappa_\parallel(v) = \frac{3v^3}{20 L_c \Omega_0^2 \sigma^2}\csc\left(\frac{3\pi}{5}\right)\left[1 + \frac{72}{7}\left(\frac{\Omega_0 L_c}{v}\right)^{5/3}\right], \quad (5)$$

where v is the particle speed, L_c is the turbulence correlation length, Ω_0 is the particle gyrofrequency, and $\sigma^2 = \langle \delta B^2 \rangle / B_0^2$ is the normalized wave variance of turbulence. The normalization of the diffusion coefficient is then $\kappa_0 = L_0 v_A = 5 \times 10^{16}\,\mathrm{cm^2\,s^{-1}}$, and the normalization of time is $t_0 = L_0/v_A = 5$ s. We assume that the correlation length L_c is equal to

a simulation box size/30 $\approx$ 333 km, which is the largest eddy size in a reconnection-driven turbulence, as shown by 3D MHD simulations of magnetic reconnection (Huang & Bhattacharjee 2016). We assume the average magnetic field $B_0 = 50$ G and $\sigma^2 = 1$. Then, $\kappa_\parallel = 1.5 \times 10^{14}\,\mathrm{cm^2\,s^{-1}}$ for 10 keV protons and $4.0 \times 10^{14}\,\mathrm{cm^2\,s^{-1}}$ for 1 keV electrons, corresponding to $0.003\kappa_0$ and $0.008\kappa_0$ using simulation units. Test-particle simulations have suggested that $\kappa_\perp/\kappa_\parallel$ is about 0.02–0.04 and nearly independent of particle energy (Giacalone & Jokipii 1999). There is also observational evidence suggesting that $\kappa_\perp/\kappa_\parallel$ can be quite large (e.g., Dwyer et al. 1997; Zhang et al. 2003). Here we examine the effect of $\kappa_\perp/\kappa_\parallel$ by adopting three different perpendicular diffusion values, $\kappa_\perp/\kappa_\parallel = 0.01, 0.05$, and 1.0.

The Parker transport equation can be solved by integrating the stochastic differential equation corresponding to the Fokker–Planck form of the transport equation (Zhang 1999; Florinski & Pogorelov 2009; Pei et al. 2010; Kong et al. 2017). Neglecting the source term Q in Equation (3) and assuming $F = fp^2$,

$$\frac{\partial F}{\partial t} = -\nabla\cdot[(\nabla\cdot\boldsymbol{\kappa}+\boldsymbol{v})F] + \frac{\partial}{\partial p}\left[\frac{p}{3}\nabla\cdot\boldsymbol{v}F\right] + \nabla\cdot(\nabla\cdot(\boldsymbol{\kappa}F)), \tag{6}$$

which is equivalent to a system of stochastic differential equations of the Ito type,

$$dX = (\nabla\cdot\boldsymbol{\kappa}+\boldsymbol{v})ds + \sum_\sigma \boldsymbol{\alpha}_\sigma dW_\sigma(s),$$
$$dp = -\frac{p}{3}(\nabla\cdot\boldsymbol{v})ds, \tag{7}$$

where $\sum_\sigma \alpha_\sigma^\mu \alpha_\sigma^\nu = 2\kappa^{\mu\nu}$, dW is the normalized distributed random number with mean zero and variance $\sqrt{\Delta t}$, and Δt is the time step for stochastic integration. This corresponds to a Wiener process. Numerical approximation is often used for the Wiener process to replace the normal distribution. We use a uniform distribution in $[-\sqrt{3}, \sqrt{3}]$ in the code. For a 2D problem,

$$\boldsymbol{\alpha}_1 = \begin{pmatrix}\sqrt{2\kappa_\perp}\\ 0\end{pmatrix},$$
$$\boldsymbol{\alpha}_2 = \begin{pmatrix}0\\ \sqrt{2\kappa_\perp}\end{pmatrix},$$
$$\boldsymbol{\alpha}_3 = \sqrt{2(\kappa_\parallel-\kappa_\perp)}\begin{pmatrix}B_x/B\\ B_y/B\end{pmatrix}. \tag{8}$$

The parameters used at particle locations are calculated from v_x, v_y, B_x, B_y, $\nabla\cdot\boldsymbol{v}$, $\partial B_x/\partial x$, $\partial B_x/\partial y$, $\partial B_y/\partial x$, and $\partial B_y/\partial y$, which are all obtained from the MHD simulations. We interpolate these parameters to the particle positions and then calculate the other required parameters:

$$\frac{\partial\kappa_{xx}}{\partial x} = \frac{\partial\kappa_\perp}{\partial x} - \frac{\partial(\kappa_\perp-\kappa_\parallel)}{\partial x}\frac{B_x^2}{B^2} - 2(\kappa_\perp-\kappa_\parallel)\frac{\frac{\partial B_x}{\partial x}B_xB - \frac{\partial B}{\partial x}B_x^2}{B^3},$$
$$\frac{\partial\kappa_{yy}}{\partial y} = \frac{\partial\kappa_\perp}{\partial y} - \frac{\partial(\kappa_\perp-\kappa_\parallel)}{\partial y}\frac{B_y^2}{B^2} - 2(\kappa_\perp-\kappa_\parallel)\frac{\frac{\partial B_y}{\partial y}B_yB - \frac{\partial B}{\partial y}B_y^2}{B^3},$$
$$\frac{\partial\kappa_{xy}}{\partial x} = -\frac{\partial(\kappa_\perp-\kappa_\parallel)}{\partial x}\frac{B_xB_y}{B^2} - (\kappa_\perp-\kappa_\parallel)\frac{\left(\frac{\partial B_x}{\partial x}B_y + B_x\frac{\partial B_y}{\partial x}\right)B - 2B_xB_y\frac{\partial B}{\partial x}}{B^3},$$
$$\frac{\partial\kappa_{xy}}{\partial y} = -\frac{\partial(\kappa_\perp-\kappa_\parallel)}{\partial y}\frac{B_xB_y}{B^2} - (\kappa_\perp-\kappa_\parallel)\frac{\left(\frac{\partial B_x}{\partial y}B_y + B_x\frac{\partial B_y}{\partial y}\right)B - 2B_xB_y\frac{\partial B}{\partial y}}{B^3},$$
$$\frac{\partial B}{\partial x} = \frac{1}{B}\left(B_x\frac{\partial B_x}{\partial x} + B_y\frac{\partial B_y}{\partial x}\right),$$
$$\frac{\partial B}{\partial y} = \frac{1}{B}\left(B_x\frac{\partial B_x}{\partial y} + B_y\frac{\partial B_y}{\partial y}\right)$$

where $\kappa_\parallel$ and $\kappa_\perp$ can be functions of B_x, B_y, and B, so $\partial\kappa_\parallel/\partial x$, $\partial\kappa_\parallel/\partial y$, $\partial\kappa_\perp/\partial x$, and $\partial\kappa_\perp/\partial y$ still depend on the derivatives $\partial B_x/\partial x$, $\partial B_x/\partial y$, $\partial B_y/\partial x$, and $\partial B_y/\partial y$. The detailed expressions depend on the diffusion model to choose.

In this work, we use a derivative-free Milstein method (Burrage et al. 2004) to solve the stochastic differential equation. It is different from the usual method due to one more term, which makes it become a higher-order method:

$$\frac{dX_t}{dt} = f(X_t, t)dt + g(X_t, t)dW_t, \tag{9}$$
$$X_{n+1} = X_n + f_n h + g_n\Delta W_n + \frac{1}{2\sqrt{h}}[g(\bar{X}_n) - g_n][(\Delta W_n)^2 - h], \tag{10}$$
$$\bar{X}_n = X_n + f_n h + g_n\sqrt{h}, \tag{11}$$
$$\Delta W_n = [W_{t+h} - W_t] \sim \sqrt{h}N(0, 1), \tag{12}$$

where X corresponds to spatial positions x, y and particle momentum p in our simulation. Here $f(X_t, t)$ is the deterministic term, $g(X_t, t)$ is the probabilistic term, h is the time step, and $N(0,1)$ indicates a normal distribution, which is substituted with a uniform distribution $[-\sqrt{3}, \sqrt{3}]$ in our simulations to speed up the computation. For a 1D problem, the particle moves a distance satisfying $l_x^2 = \max(\langle\Delta x\rangle^2, \langle\Delta x^2\rangle)$ (Strauss & Effenberger 2017), where

$$\langle\Delta x\rangle = \left(v_x + \frac{d\kappa(x)}{dx}\right)\Delta t, \quad \langle\Delta x^2\rangle = 2\kappa(x)\Delta t, \tag{13}$$

and l_x should be much smaller than the spatial variation scale of the fields. In this work, we assume $\langle\Delta x\rangle^2 < \langle\Delta x^2\rangle$ and choose

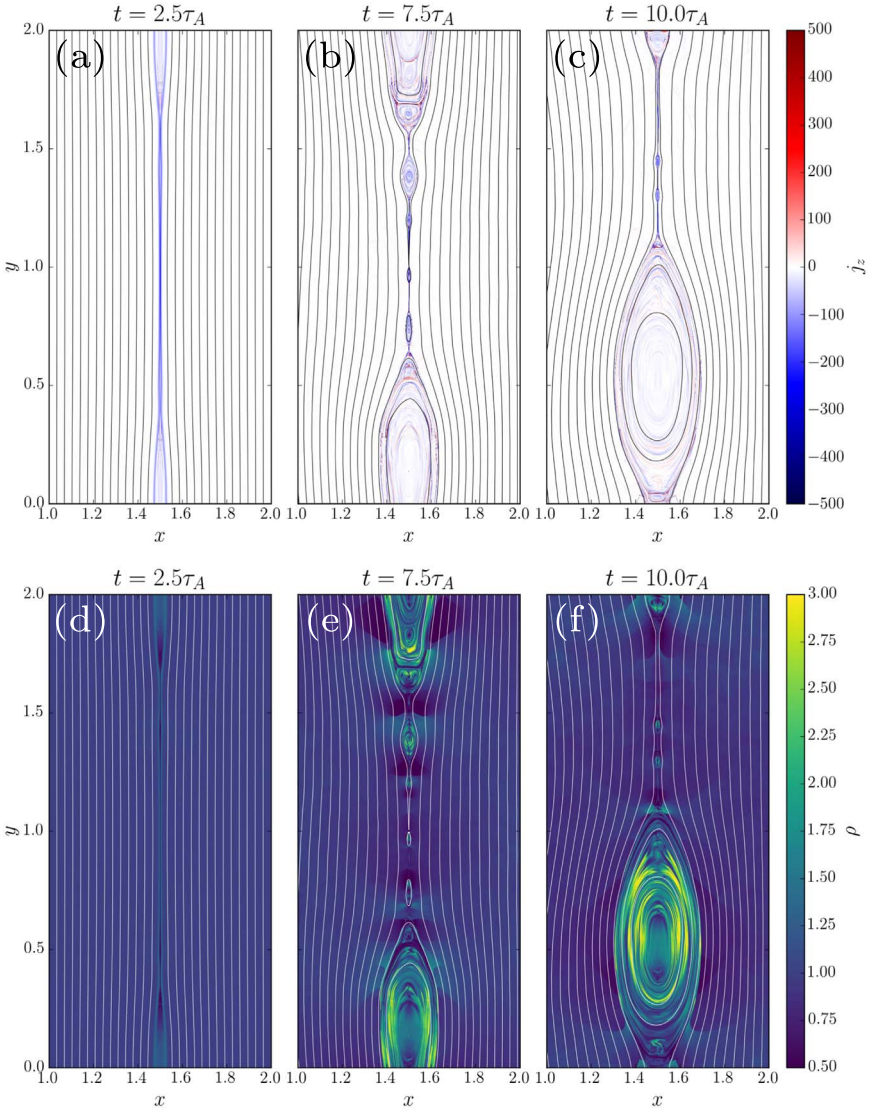

Figure 1. Out-of-plane current density j_z and plasma density ρ at $t = 2.5\tau_A$, $7.5\tau_A$, and $10\tau_A$ for half of the simulation box ($x = 1.0$–2.0), where τ_A is the Alfvén crossing time L_y/v_A. The initial plasma density ≈1.0.

Δt so that $l_x \ll \delta_x$, where δ_x is the grid size. For our 2D problems, we choose the following criteria to determine the time step:

$$\Delta t_x = \min\left[\frac{\delta x}{80|v_x + \partial_x\kappa_{xx} + \partial_y\kappa_{xy}|}, \frac{(\sqrt{2\kappa_\perp} + \sqrt{2(\kappa_\parallel - \kappa_\perp)}\,|B_x/B|)^2}{|v_x + \partial_x\kappa_{xx} + \partial_y\kappa_{xy}|^2}\right], \quad (14)$$

$$\Delta t_y = \min\left[\frac{\delta y}{80|v_y + \partial_y\kappa_{yy} + \partial_x\kappa_{xy}|}, \frac{(\sqrt{2\kappa_\perp} + \sqrt{2(\kappa_\parallel - \kappa_\perp)}\,|B_y/B|)^2}{|v_y + \partial_y\kappa_{yy} + \partial_x\kappa_{xy}|^2}\right], \quad (15)$$

$$\Delta t = \min(\Delta t_x, \Delta t_y). \quad (16)$$

3. Results

3.1. Compression in a Reconnection Layer

As reconnection evolves, the current sheet becomes thinner and eventually unstable to the plasmoid instability (Loureiro et al. 2007; Bhattacharjee et al. 2009; Comisso et al. 2016). Figure 1 shows the time evolution of the out-of-plane current density j_z and plasma density ρ. At $t = 2.5\tau_A$, where τ_A is the Alfvén crossing time L_y/v_A, the current sheet just starts to break into magnetic islands (Figures 1(a) and (d)). These magnetic islands tend to contract due to magnetic tension force and merge with each other to form larger islands ($t = 7.5\tau_A$ and $10\tau_A$). Figures 1(b) and (c) show that new islands are continuously generated in the unstable current sheet. During these processes, the maximum plasma density increases from 1.0 to 3.0 or higher (Figures 1(e) and (f)). The regions with enhanced density are concentrated in magnetic islands, reconnection exhaust, and inflow regions around the top and bottom sides of the magnetic islands. Due to the mass conservation in the simulation domain, density decreases in the inflow regions close to the reconnection layer and some regions in

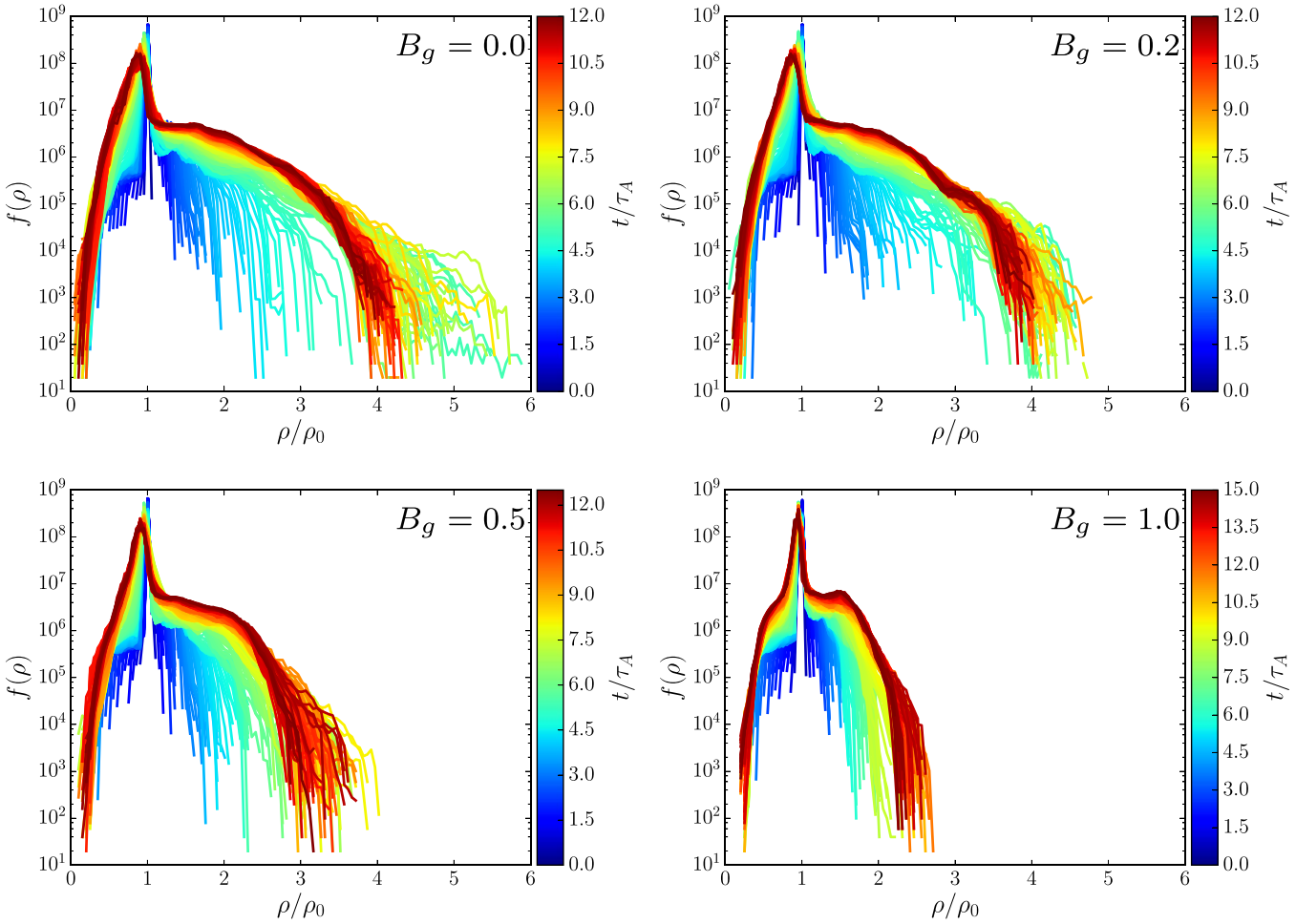

Figure 2. Time evolution of the density distributions for runs with different guide fields. The plasma density is normalized by the initial values in each simulation. Time t is normalized by the Alfvén crossing time $\tau_A = L_y/v_A$.

the islands. Particles can be accelerated or decelerated when crossing these regions. We expect that the net effect will be acceleration because, on average, the density increases as particles move from the inflow to the outflow regions.

The enhanced plasma density suggests that the plasma in the reconnection layer is compressed. To further examine the plasma compressibility, Figure 2 shows the time evolution of the density distributions $f(\rho)$ for different runs. Plasma density evolves to have a broad distribution from an initially nearly uniform value ρ_0. The distributions constantly change as the simulation evolves, suggesting that the reconnection layer is very dynamic. Take the run with $B_g = 0$, for example, where ρ/ρ_0 reaches about 6 and then decreases to about 4, suggesting that the compressed plasma in the reconnection layer can expand at a late stage. Due to the mass conservation, Figure 2 shows significant distribution with $\rho/\rho_0 < 1$. The guide field plays an important role in controlling the plasma compressibility. As B_g increases, the maximum density decreases from about 6 when $B_g = 0.0$ to 2.7 when $B_g = 1.0$. This result is consistent with previous MHD simulations (Birn et al. 2012; Provornikova et al. 2016). Note that $f(\rho)$ for $B_g = 0.2$ is close to the case with $B_g = 0$, indicating that a weak guide field is not dynamically important here. This is because the magnetic pressure from the guide-field component is only 0.04 times that of the reconnecting component. The broad $f(\rho)$ and the nonuniform spatial distribution of ρ indicate that not all particles can "see" the entire density transition and that the particle energy spectrum might not be a simple function of the compression ratio, as predicted by diffusion–advection analysis in a planar current sheet (Drury 2012).

3.2. Particle Acceleration Due to Compression: Constant Diffusion Coefficients

The onset time for fast reconnection varies with the guide field. Since we are mostly interested in the phase when the plasmoid instability is developed, we start solving the acceleration of energetic particles by injecting pseudoparticles into the simulation when a strong reconnection electric field emerges. Figure 3 shows the time evolution of the maximum value of the reconnection electric field $|\eta j_z|$, where η is the resistivity. Here $|\eta j_z|_{\max}$ starts growing at different times as the guide field varies. For runs with $B_g = 0$ and 0.2, the rise time is almost the same. For runs with higher B_g, it takes longer for $|\eta j_z|_{\max}$ to grow. Based on this result, we inject particles at $2\tau_A$ when $B_g = 0$ or 0.2, at $2.5\tau_A$ when $B_g = 0.5$, and at $5\tau_A$ when $B_g = 1.0$. For all the simulation cases, we continue to run the simulation for $10\tau_A$ and solve the transport equation.

We now discuss the results of energetic particle acceleration. Figure 4 shows the final particle energy spectra when using constant diffusion coefficients. We show two sets of simulations, one for protons with an initial energy of 10 keV and

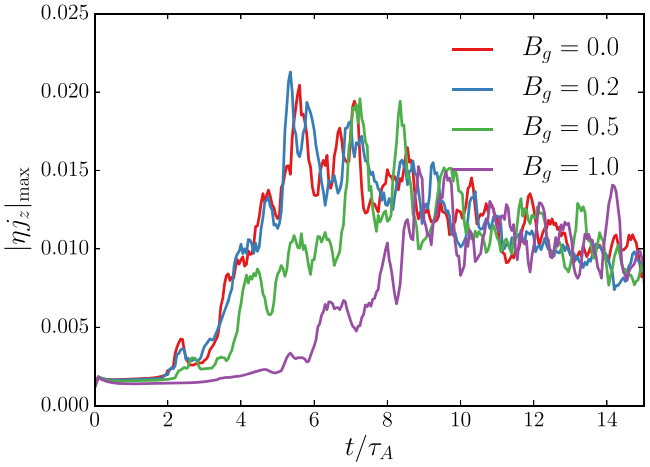

Figure 3. Time evolution of the maximum of $|\eta j_z|$ for different runs, where η is the resistivity and j_z is the out-of-plane current density.

$\kappa_\parallel = \kappa_\perp = 0.003\kappa_0$ (Figure 4(a)) and the other for electrons with an initial energy of 1 keV and $\kappa_\parallel = \kappa_\perp = 0.008\kappa_0$ (Figure 4(b)). The eventual particle energy spectra resemble power-law distributions. When the guide field is weak, the power-law distributions extend several orders of magnitude in energy. As the guide field gets stronger, the power-law spectra become steeper and shorter, indicating that particle acceleration is more efficient in the reconnection with a weaker guide field. The spectra are close to each other for cases with $B_g = 0$ and 0.2. This is because the compressibilities of the two cases are close to each other (Figure 2). When B_g increases to 1.0, the particle spectrum becomes very steep, with $f(\varepsilon) \sim \varepsilon^{-8.45}$ for protons and $f(\varepsilon) \sim \varepsilon^{-12.1}$ for electrons, and the maximum energy is less than 10 times the initial particle energy. These results show that the guide-field strength is critical for particle acceleration during magnetic reconnection. When the guide field is weak, the plasma is strongly compressed in the reconnection layer, leading to an energy spectrum harder than that of the strong guide-field case. This trend for the relation between the spectral index and the compressed plasma density is in agreement with Drury (2012), except that the spectral index also has a weak dependence on the diffusion coefficient.

To examine the nature of particle acceleration in a reconnection layer, we then study how the particle acceleration rate depends on the flow speed, which is about the Alfvén speed v_A in a reconnection layer. We add another three simulations with fixed $\kappa_\parallel = \kappa_\perp = 1.5 \times 10^{14}\,\mathrm{cm^2\,s^{-1}}$ and $L_0 = 5000\,\mathrm{km}$ but different v_A from 300 to $10^4\,\mathrm{km\,s^{-1}}$ for the MHD run with $B_g = 0$. The normalized $\kappa_\parallel$ and $\kappa_\perp$ then change from $0.01\kappa_0$ to $3 \times 10^{-4}\kappa_0$. For each pseudoparticle, we calculate the acceleration rate $dp/dt = \Delta p/\Delta t$ for each short time interval $\Delta t = 0.0005\tau_A$. Then, we statistically calculate the acceleration rate for all particles in the system. Figure 5(a) shows the distributions of $\langle dp/d\tilde{t}\rangle$, averaged from $t = 2\tau_A$ to $12\tau_A$, where we have normalized the simulation time t with L_0/v_{A0}, and v_{A0} is $300\,\mathrm{km\,s^{-1}}$ in our normalization. The measured acceleration rate is close to zero near the injected momentum, since most of the injected pseudoparticles are outside of the reconnection layer in the beginning. At higher energies, the acceleration rate becomes a power-law-like distribution as a function of momentum $\langle dp/d\tilde{t}\rangle = C(p/p_0)^\alpha$. The acceleration rate index α is 1.06–1.10, which is expected as particles gain energy through the compression term $-p\nabla\cdot\boldsymbol{v}/3$ in the Parker transport equation. Figure 5(a) also shows that the acceleration rate increases when the Alfvén speed gets larger. To further study the scaling of the acceleration rate with respect to v_A, we fit C as a function of v_A in Figure 5(b). We find the acceleration rate normalization $C \propto (v_A/v_{A0})^{1.36}$, where v_{A0} is $300\,\mathrm{km\,s^{-1}}$ in our normalization, suggesting that the acceleration mechanism is a mixture of a first-order Fermi mechanism ($\propto V/c$; e.g., Blandford & Eichler 1987) and second-order Fermi mechanism ($\propto (V/c)^2$; Fermi 1949), where V is the fluid speed ($\sim v_A$ in reconnection) and is typically much smaller than the light speed c. This is because particles can gain energy in the compression region and lose energy in the expansion region in the reconnection layer. If the compression region and expansion region are uniformly distributed in the reconnection layer, particles will experience a second-order Fermi acceleration similar to the original idea of Fermi (1949). Instead, on average, particles experience a net compression as they move into the reconnection layer, where plasma is strongly compressed, as shown in Figure 1. Since the reconnection layer is dynamically evolving, the acceleration rate is time-dependent as well. Figures 5(c) and (d) show the time evolution of the acceleration rate index α and acceleration rate normalization C. The α index fluctuates throughout the simulation. For the three cases with stronger acceleration, the power-law index fluctuates around 1.1. For the case with $v_A = 300\,\mathrm{km\,s^{-1}}$, the index is larger, which is likely due to statistical errors, as only a small number of particles are accelerated to high energy. Figure 5(d) shows that the acceleration rate generally decreases as the simulation evolves, which is likely because reconnection becomes saturated in the late stage.

3.3. Particle Acceleration Due to Compression: Energy-dependent Diffusion Coefficients

The constant and isotropic diffusion coefficient is a simplified assumption. In reality, κ usually depends on particle momentum. According to the quasi-linear theory (Equation (5)), $\kappa_\parallel \sim p^{4/3}$ for nonrelativistic particles propagating in magnetic turbulence with a Kolmogorov power spectrum. The diffusion coefficient in directions parallel and perpendicular to the magnetic field can be quite different, and previous test-particle calculations give a perpendicular diffusion coefficient of about a few percent of the parallel diffusion. Figure 6 shows the final energy spectra when we use energy-dependent $\kappa_\parallel = \kappa_1(p/p_0)^{4/3}$ ($\kappa_1 = 0.008\kappa_0$ for electrons and $0.003\kappa_0$ for protons) with three different $\kappa_\perp/\kappa_\parallel$: $\kappa_\perp = \kappa_\parallel$, $\kappa_\perp = 0.05\kappa_\parallel$, and $\kappa_\perp = 0.01\kappa_\parallel$. The figure shows several trends. First, particles still develop power-law energy spectra, but the power-law energy range is shorter, and the spectra roll over at certain energies depending on the diffusion model. The maximum particle energies are lower compared with the case with constant κ because high-energy particles can escape from the acceleration regions much more easily due to their larger diffusion coefficients. Second, as the ratio $\kappa_\perp/\kappa_\parallel$ decreases, the spectra become harder, and the maximum energy is higher. The spectra change dramatically for cases with $B_g = 1.0$. The power-law index s changes from $s \sim 8.5$ to $s \sim 4$ for protons and from $s \sim 12$ to $s \sim 4.5$. This is because when cross-field diffusion gets smaller, particles could stay in the acceleration regions for a longer time. Third, the maximum energies get close for cases with weak or moderate guide fields ($B_g \leqslant 0.5$), even though the power-law part is steeper for cases with higher guide fields. Finally, in all cases, protons can be accelerated to

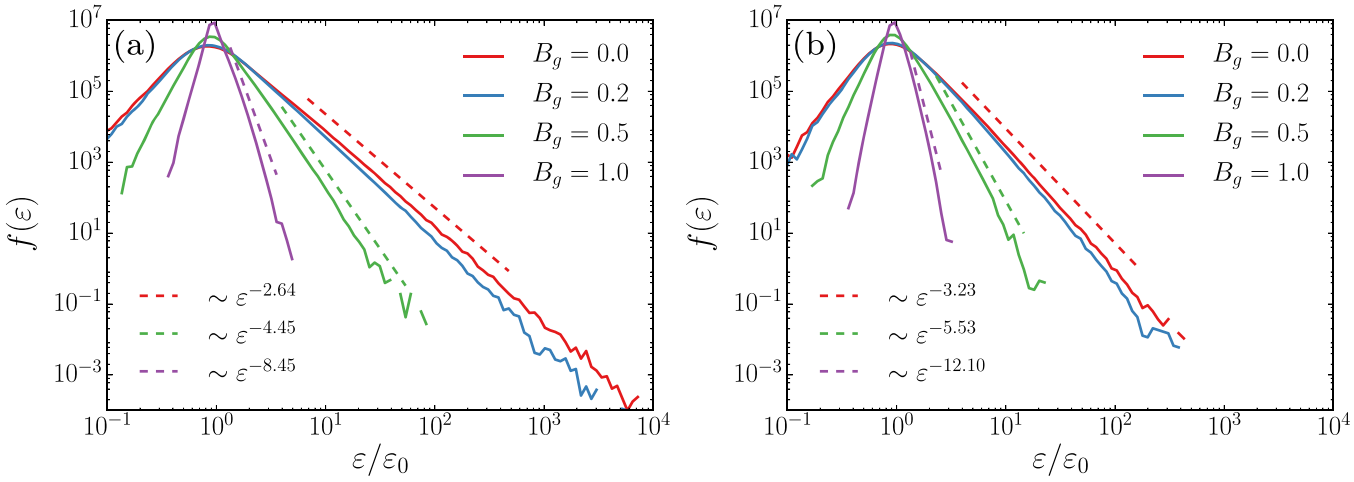

Figure 4. Particle energy distributions for cases with constant diffusion coefficients. Here p is the particle momentum, and ε indicates the particle energy and is normalized by the initial particle energy ε_0. The dashed lines indicate power-law fittings. For panel (a), we assume that the particles are protons with an initial energy of 10 keV and $\kappa_\parallel = \kappa_\perp = 0.003\kappa_0$. For panel (b), we assume that the particles are electrons with an initial energy of 1 keV and $\kappa_\parallel = \kappa_\perp = 0.008\kappa_0$.

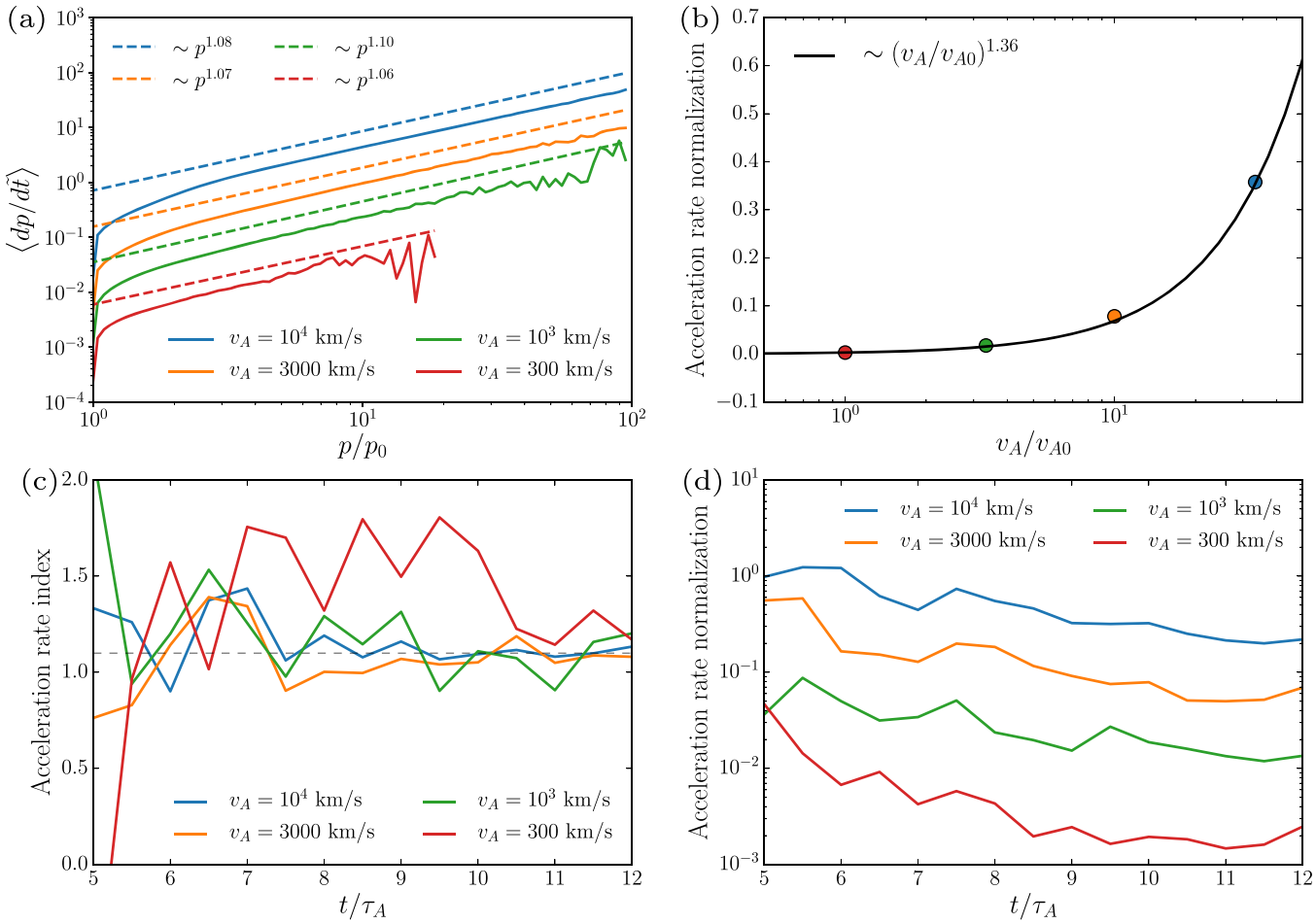

Figure 5. Diagnostics on particle acceleration rate for simulations with constant κ. We vary the value of κ by changing the Alfvén speed v_A and keeping the length scale L_0 constant. Here we use the MHD run with $B_g = 0$. (a) The $\langle dp/d\tilde{t} \rangle$ as a function of particle momentum. Note that we have normalized the simulation time t in all runs with L_0/v_{A0}, which is 300 km s^{-1} in our normalization, so $\tilde{t} = tv_{A0}/L_0$. We accumulate dp/dt and particle number n_p in each momentum bin every $0.0005\tau_A$ from $2\tau_A$ to $12\tau_A$ and calculate $\langle dp/d\tilde{t} \rangle = (\sum dp/dt)v_A/(n_p v_{A0})$. The solid lines are simulation data, and the dashed lines are the power-law fittings Cp^α, where C is the acceleration rate normalization and α is the acceleration rate index. Note that the power-law fitting is shifted for better visualization. (b) Scaling of C and hence $\langle dp/d\tilde{t} \rangle$ with respect to v_A. The four dots correspond to the four runs in panel (a). The black solid line is the power-law fitting. We normalize v_A by v_{A0}. (c) Time evolution of the acceleration rate index starting at $t = 5\tau_A$, when particles can be accelerated to fairly high energies. The black dashed line indicates an acceleration rate index of 1.1. (d) Time evolution of the acceleration rate normalization C.

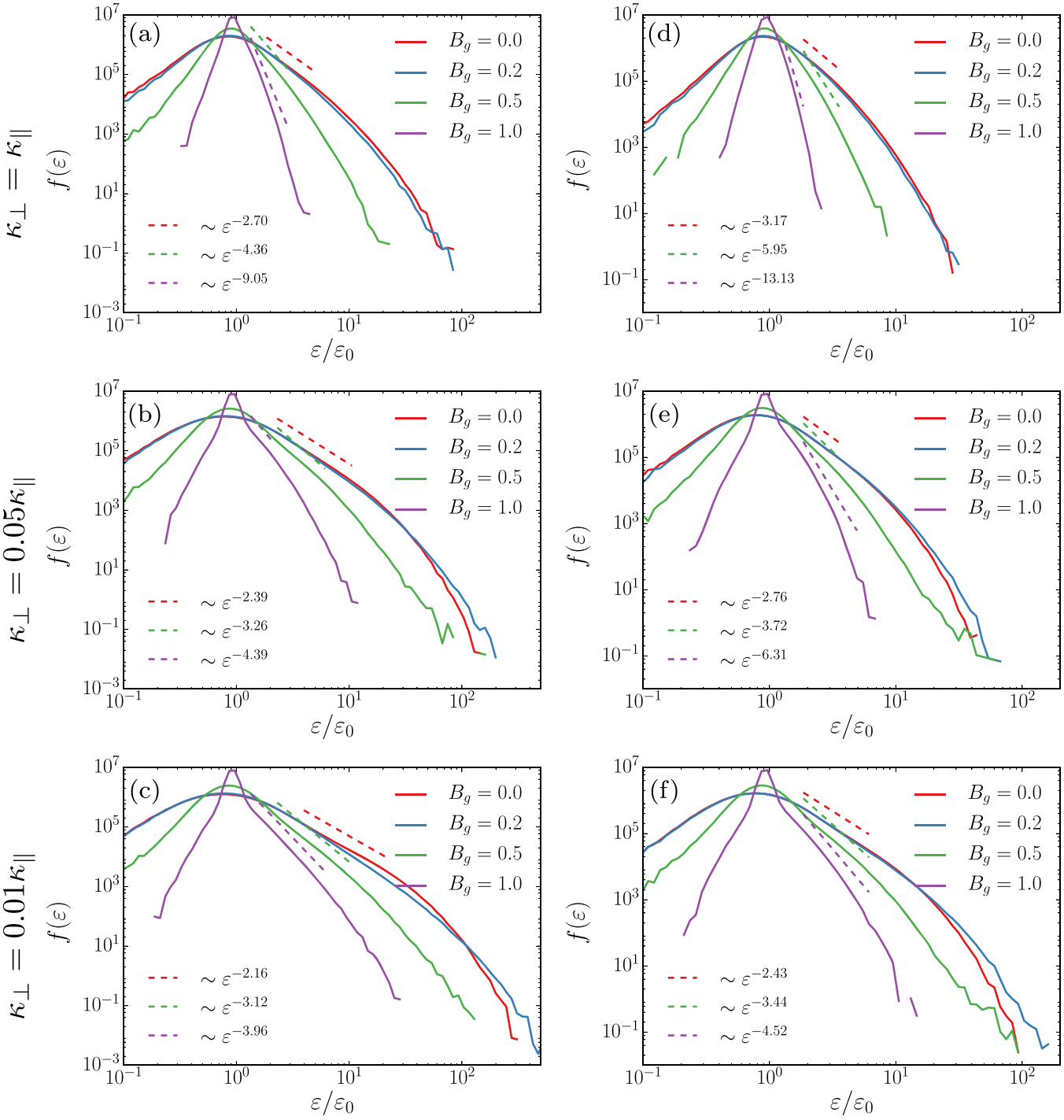

Figure 6. Particle energy distributions when $\kappa \propto p^{4/3}$ for cases with different $\kappa_\perp/\kappa_\parallel$. For panels (a)–(c), we assume that the particles are protons with an initial energy 10 keV and initial $\kappa_\parallel = 0.003\kappa_0$. For panels (d)–(f), we assume that the particles are electrons with an initial energy 1 keV and initial $\kappa_\parallel = 0.008\kappa_0$.

hundreds of keV, and electrons can be accelerated to tens of keV. For the case with $\kappa_\perp = 0.01\kappa_\parallel$, protons are accelerated to a few MeV, and electrons are accelerated to 100 keV, which is consistent with solar flare observations.

The accelerated particles are not uniformly distributed in the simulations. Figure 7 shows the spatial distributions of high-energy electrons (9–36 keV) for the simulation using the MHD run with $B_g = 0$, $\kappa_\parallel = 0.008\kappa_0$, and $\kappa_\perp = 0.01\kappa_\parallel$. At an earlier time ($t = 7.5\tau_A$), high-energy electrons are mostly in the island at $y \sim 1.4$, the top side of the large island at $y \sim 0.5$, and the island-merging region at $y \sim 1.65$, suggesting that these regions are efficient at accelerating particles. As the simulation evolves, high-energy particles are advected with reconnection outflow and diffuse to broader regions. Close to the end of the simulation ($t = 10\tau_A$), high-energy particles become more uniform, but their distribution still peaks at the two ends of the large magnetic island and in the reconnection exhaust. This geometry is similar to the above-the-loop-top hard X-ray sources observed in solar flares (Krucker et al. 2010; Oka et al. 2015). The confinement of high-energy electrons could potentially explain the hard X-ray emission observed by *RHESSI*.

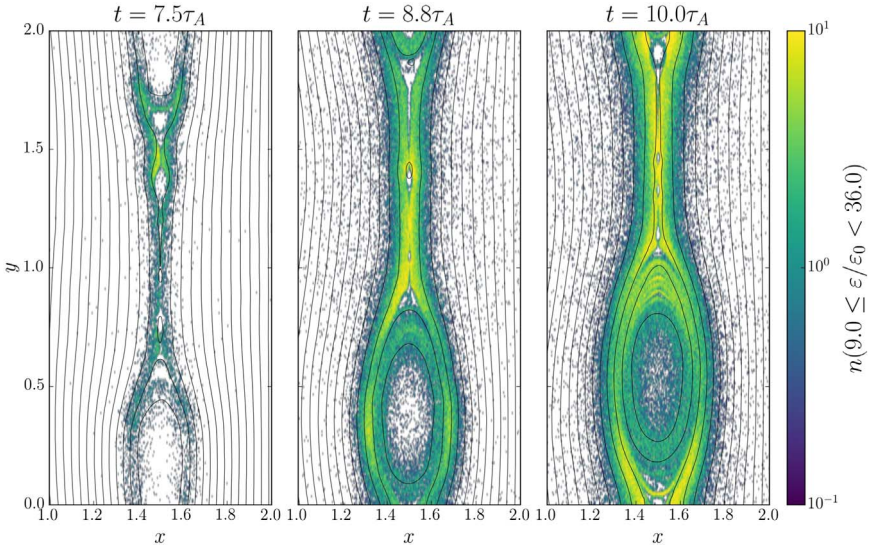

Figure 7. Spatial distributions of high-energy particles for the MHD run without a guide field at $t = 7.5\tau_A$, $8.8\tau_A$, and $10.0\tau_A$. Here we assume that the particles are electrons with an initial energy $\varepsilon_0 = 1$ keV, $\kappa_\parallel = 0.008\kappa_0$, and $\kappa_\perp/\kappa_\parallel = 0.01$. We choose particles with energy $9.0 \leqslant \varepsilon/\varepsilon_0 < 36.0$.

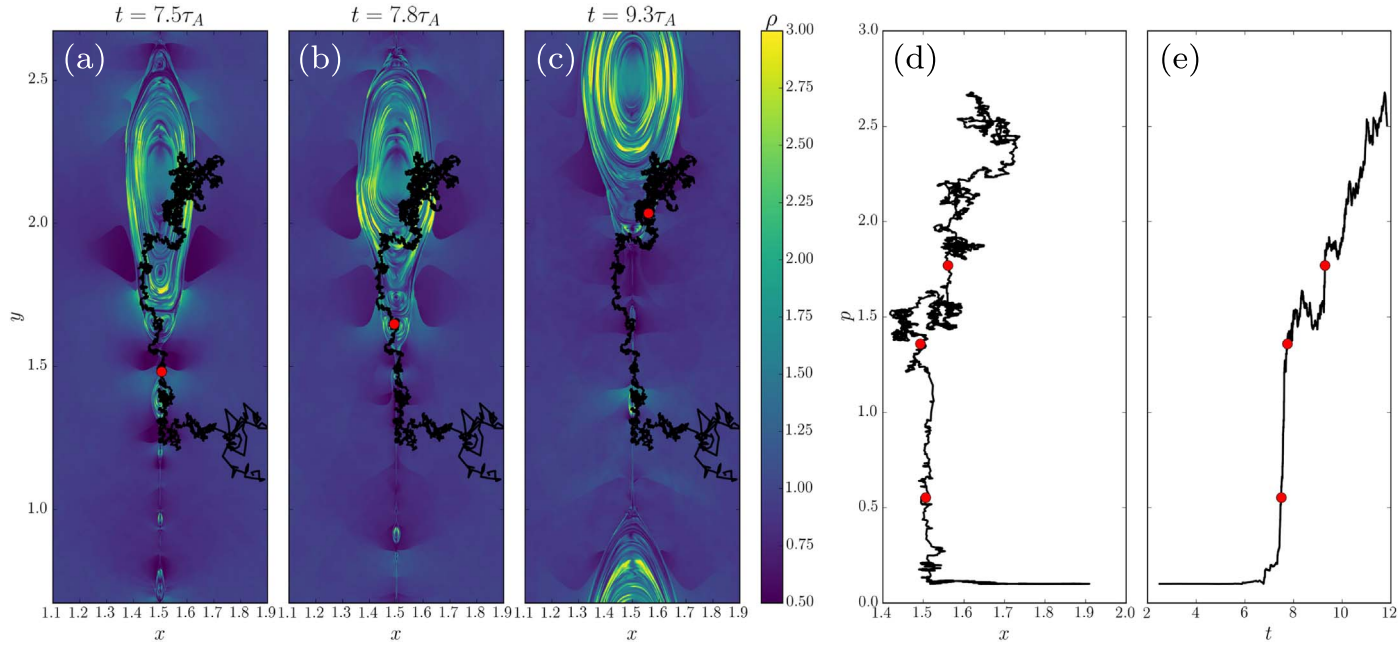

Figure 8. Pseudoparticle trajectory in the case with a constant $\kappa = 0.003\kappa_0$ and the MHD simulation without a guide field. Panels (a)–(c) show the trajectory with plasma density ρ as background at three different time frames. The initial plasma density ≈1.0. The red dots indicate the particle positions at each time frame. Panel (d) shows the particle momentum vs. x position. Panel (e) shows the particle momentum vs. time. The three red dots indicate the three time frames shown in panels (a)–(c). The initial particle momentum is 0.1. Since we use periodic boundary conditions, we have shifted the background and particle trajectory when the particle crossed the boundary at $y = 2.0$ for better visualization.

3.4. Trajectories of Pseudoparticles

To further illustrate how particles are accelerated, Figure 8 shows a representative pseudoparticle trajectory in the case with a constant $\kappa = 0.003\kappa_0$ and without a guide field. Three red dots indicate the three major acceleration phases, including reconnection exhaust, contracting islands, and island-merging regions. Initially, the particle slowly gets advected into the reconnection layer. It gains energy in a short period of time ($7\tau_A < t < 8\tau_A$) when the particle diffuses across the reconnection current sheet, where the background plasma is highly compressed. This indicates that the particle acceleration in reconnection exhaust is dominated by a first-order Fermi process. The particle is then trapped in a magnetic island and gains more energy, but the rate of energy increase becomes lower. This is because particles can lose energy when they cross expanding regions of the magnetic island (Figure 1). In the late phase, the small island merges with the large island, and the particle gets accelerated and decelerated multiple times but still gains more energy on average. These results indicate that particle acceleration in contracting islands and island-merging regions is a mixture of first- and second-order Fermi processes but is dominated by the first-order process. This is due to the multiple compression and expansion layers in these regions and the oscillations caused by merging magnetic islands. Note that the contracting island is a favorable region

for the first-order Fermi acceleration, but the pseudoparticle trajectory shows that the contracting island (Figure 8(b) and the middle red dot in panels (d) and (e)) is not the dominant mechanism. Some other trajectories do show that the contracting island can be the dominant acceleration process (not shown here).

4. Discussion and Conclusion

In this work, we have studied particle acceleration in a large-scale reconnection site through solving the Parker energetic particle transport equation using velocity and magnetic fields from MHD simulations of high-Lundquist-number magnetic reconnection. We found that compression in the reconnection layer leads to significant particle acceleration and the formation of power-law energy distributions for both electrons and ions. As the guide field becomes stronger, the power-law distribution gets steeper, and the energy rollover of the power-law distribution and maximum particle energy decrease. The power-law index for electrons is about 2.4–13.1, depending on the guide-field strength, which is close to the range found in solar flare observations (Effenberger et al. 2017; Oka et al. 2018) and the observations of electron SEP events (Krucker et al. 2007, 2009). The strong dependence of particle acceleration on the guide field may be tested in observations (e.g., Qiu et al. 2010). When the perpendicular spatial diffusion is much smaller than the parallel diffusion, we found that the maximum electron energy reaches $\sim$100 keV and the maximum proton energy reaches a few MeV. Detailed analysis shows that the acceleration rate $\propto v_{\rm A}^{1.36}$, indicating a mixture of first- and second-order Fermi processes. Pseudoparticle trajectories show that the particle acceleration in reconnection exhaust is dominated by first-order Fermi processes and that the acceleration in contracting and merging magnetic islands is a mixture of first- and second-order Fermi processes but still dominated by first-order Fermi processes.

Our simulations also generate 2D spatial distributions of energetic particles. We found that the energetic particles are concentrated in reconnection exhaust and magnetic islands. If combined with a radiation model, the 2D distributions could be used to make a predicted radiation map that is comparable with hard X-ray observations by *RHESSI* and *FOXSI* and microwave imaging by radio observatories such as the Very Large Array and Expanded Owens Valley Solar Array (Gary et al. 2018).

Our results are consistent with those of Drury (2012), who showed that the spectral index depends on the compressibility of the reconnection layer. But we found that the spectral index is not just a simple expression of the compression ratio between the outflow and inflow regions. This is likely due to the complex structures (e.g., magnetic islands) and multiple compression and expansion regions formed in the reconnection layer. We found in our simulations that the particle energy spectra depend on the diffusion model, especially the ratio of the perpendicular and parallel diffusion coefficients. Particle diffusion processes depend on the properties of turbulence in the reconnection region, such as the turbulence spectrum, turbulence amplitude, correlation length, and turbulence anisotropy, which are still under active research (Huang & Bhattacharjee 2016; Beresnyak 2017; Boldyrev & Loureiro 2017; Kowal et al. 2017; Loureiro & Boldyrev 2017a, 2017b; Mallet et al. 2017; Comisso et al. 2018; Dong et al. 2018; Walker et al. 2018). We expect a better understanding of these turbulence properties and hence the particle diffusion processes in a reconnection layer in the near future.

Our results are also consistent with in situ observations in Earth's magnetotail. Specifically, using spacecraft measurements, Fu et al. (2013b) found that the reconnection layer is compressible and plasmoids are easily formed in this compressible layer; Fu et al. (2013a) pointed out that the compressibility of the reconnection layer can affect the contraction of magnetic islands and hence the electron acceleration efficiency.

While fluid compression is the only acceleration mechanism considered in this study, incompressible effects (e.g., fluid shear) could also accelerate particles (Drake et al. 2006; Zank et al. 2014; le Roux et al. 2015; Li et al. 2018), potentially leading to stronger particle acceleration than that in observations. Quantifying how other mechanisms change the particle spectral shape and maximum energies may be important for future studies.

The developed numerical tools are not limited to studying particle acceleration in large solar flares. They can also be used to study particle acceleration at the reconnection sites of nanoflares, which have been proposed as a candidate for explaining the power-law energy spectrum of superhalo electrons in the solar wind at quiet times (Wang et al. 2012, 2015). We defer this to a future work.

Our 2D simulations have a few limitations. First, the periodic boundary conditions allow the large island to grow to the system size, while in a solar flare, the largest island is likely to be ejected out of the reconnection layer and cannot grow to the system size; thus, the current boundary conditions might lead to stronger particle acceleration. Second, the 2D configuration prevents the field variation along the out-of-plane direction, which might affect the compression energization that depends on the divergence of fluid velocity. Third, we use a plasma $\beta = 0.1$ instead of a lower plasma β, which may be present for solar flares, due to technical difficulties when doing high Lundquist number simulations. Lower plasma β might lead to stronger compression and hence stronger particle acceleration.

To conclude, we find that fluid compression in a reconnection layer leads to significant particle acceleration and the formation of power-law energy distributions for both electrons and ions. The compressibility of the reconnection region, which depends on the guide field, determines the spectral index and cutoff energy of the power-law distribution and the maximum particle energy. The diffusion coefficient and its anisotropy also influence the key features of the nonthermal particle spectra. Our analysis shows that the acceleration in the reconnection layer is a mixture of first- and second-order Fermi processes. Our model includes the acceleration mechanism derived from fully kinetic PIC simulations (Li et al. 2018) and also applies to a macroscopic reconnection layer like in a solar flare. The resulting time-dependent spatial and energy distributions of energetic particles can provide explanations for observed energetic particle emissions in solar flares and other astrophysical regimes.

This work was supported by NASA grant NNH16AC60I. F.G. acknowledges support in part from the National Science Foundation under grant No. 1735414 and the U.S. Department of Energy, Office of Science, Office of Fusion Energy Science, under award Number DE-SC0018240. We also acknowledge support by the DOE through the LDRD program at LANL. Simulations were performed with LANL institutional computing.

ORCID iDs

Xiaocan Li https://orcid.org/0000-0001-5278-8029
Fan Guo https://orcid.org/0000-0003-4315-3755
Hui Li https://orcid.org/0000-0003-3556-6568
Shengtai Li https://orcid.org/0000-0002-4142-3080

References

Beresnyak, A. 2017, ApJ, 834, 47
Bhattacharjee, A., Huang, Y.-M., Yang, H., & Rogers, B. 2009, PhPl, 16, 112102
Birn, J., Battaglia, M., Fletcher, L., Hesse, M., & Neukirch, T. 2017, ApJ, 848, 116
Birn, J., Borovsky, J. E., & Hesse, M. 2012, PhPl, 19, 082109
Blandford, R., & Eichler, D. 1987, PhR, 154, 1
Boldyrev, S., & Loureiro, N. F. 2017, ApJ, 844, 125
Burrage, K., Burrage, P. M., & Tian, T. 2004, RSPSA, 460, 373
Comisso, L., Huang, Y.-M., Lingam, M., Hirvijoki, E., & Bhattacharjee, A. 2018, ApJ, 854, 103
Comisso, L., Lingam, M., Huang, Y.-M., & Bhattacharjee, A. 2016, PhPl, 23, 100702
Dahlin, J. T., Drake, J. F., & Swisdak, M. 2014, PhPl, 21, 092304
Daughton, W., Roytershteyn, V., Albright, B. J., et al. 2009, PhRvL, 103, 065004
Dong, C., Wang, L., Huang, Y.-M., Comisso, L., & Bhattacharjee, A. 2018, arXiv:1804.07361
Drake, J. F., Shay, M. A., Thongthai, W., & Swisdak, M. 2005, PhRvL, 94, 095001
Drake, J. F., Swisdak, M., Che, H., & Shay, M. A. 2006, Natur, 443, 553
Drake, J. F., Swisdak, M., & Fermo, R. 2013, ApJL, 763, L5
Drury, L. O. 2012, MNRAS, 422, 2474
Dwyer, J. R., Mason, G. M., Mazur, J. E., et al. 1997, ApJL, 490, L115
Earl, J. A., Jokipii, J. R., & Morfill, G. 1988, ApJL, 331, L91
Effenberger, F., Rubio da Costa, F., Oka, M., et al. 2017, ApJ, 835, 124
Egedal, J., Daughton, W., & Le, A. 2012, NatPh, 8, 321
Egedal, J., Daughton, W., Le, A., & Borg, A. L. 2015, PhPl, 22, 101208
Egedal, J., Le, A., & Daughton, W. 2013, PhPl, 20, 061201
Fermi, E. 1949, PhRv, 75, 1169
Florinski, V., & Pogorelov, N. V. 2009, ApJ, 701, 642
Fu, H. S., Cao, J. B., Khotyaintsev, Y. V., et al. 2013b, GeoRL, 40, 6023
Fu, H. S., Khotyaintsev, Y. V., André, M., & Vaivads, A. 2011, GeoRL, 38, L16104
Fu, H. S., Khotyaintsev, Y. V., Vaivads, A., et al. 2012, JGRA, 117, A12221
Fu, H. S., Khotyaintsev, Y. V., Vaivads, A., Retinò, A., & André, M. 2013a, NatPh, 9, 426
Fu, H. S., Vaivads, A., Khotyaintsev, Y. V., et al. 2017, GeoRL, 44, 37
Fu, X. R., Lu, Q. M., & Wang, S. 2006, PhPl, 13, 012309
Gary, D. E., Chen, B., Dennis, B. R., et al. 2018, ApJ, 863, 83
Giacalone, J., & Jokipii, J. R. 1999, ApJ, 520, 204
Gordovskyy, M., Browning, P. K., & Vekstein, G. E. 2010a, A&A, 519, A21
Gordovskyy, M., Browning, P. K., & Vekstein, G. E. 2010b, ApJ, 720, 1603
Guo, F., Li, H., Daughton, W., & Liu, Y.-H. 2014, PhRvL, 113, 155005
Guo, F., Liu, Y.-H., Daughton, W., & Li, H. 2015, ApJ, 806, 167
Hoshino, M., Mukai, T., Terasawa, T., & Shinohara, I. 2001, JGR, 106, 25979
Huang, Y.-M., & Bhattacharjee, A. 2010, PhPl, 17, 062104
Huang, Y.-M., & Bhattacharjee, A. 2016, ApJ, 818, 20
Ji, H., & Daughton, W. 2011, PhPl, 18, 111207
Jokipii, J. R. 1971, RvGSP, 9, 27
Jones, F. C. 1990, ApJ, 361, 162
Kong, X., Guo, F., Giacalone, J., Li, H., & Chen, Y. 2017, ApJ, 851, 38
Kowal, G., Falceta-Gonçalves, D. A., Lazarian, A., & Vishniac, E. T. 2017, ApJ, 838, 91
Krucker, S., Hudson, H. S., Glesener, L., et al. 2010, ApJ, 714, 1108
Krucker, S., Kontar, E. P., Christe, S., & Lin, R. P. 2007, ApJL, 663, L109
Krucker, S., Oakley, P. H., & Lin, R. P. 2009, ApJ, 691, 806
Le, A., Daughton, W., Ohia, O., et al. 2018, PhPl, 25, 062103
le Roux, J. A., & Webb, G. M. 2009, ApJ, 693, 534
le Roux, J. A., Zank, G. P., Webb, G. M., & Khabarova, O. 2015, ApJ, 801, 112
Li, X., Guo, F., Li, H., & Birn, J. 2018, ApJ, 855, 80
Li, X., Guo, F., Li, H., & Li, G. 2015, ApJL, 811, L24
Li, X., Guo, F., Li, H., & Li, G. 2017, ApJ, 843, 21
Lin, R. P. 2011, SSRv, 159, 421
Lin, R. P., & Hudson, H. S. 1976, SoPh, 50, 153
Liu, C. M., Fu, H. S., Cao, J. B., et al. 2017a, GeoRL, 44, 10116
Liu, C. M., Fu, H. S., Xu, Y., Cao, J. B., & Liu, W. L. 2017b, GeoRL, 44, 6492
Liu, W., Li, H., Yin, L., et al. 2011, PhPl, 18, 052105
Liu, Y.-H., Daughton, W., Karimabadi, H., Li, H., & Roytershteyn, V. 2013, PhRvL, 110, 265004
Loureiro, N. F., & Boldyrev, S. 2017a, ApJ, 850, 182
Loureiro, N. F., & Boldyrev, S. 2017b, PhRvL, 118, 245101
Loureiro, N. F., Schekochihin, A. A., & Cowley, S. C. 2007, PhPl, 14, 100703
Mallet, A., Schekochihin, A. A., & Chandran, B. D. G. 2017, JPlPh, 83, 905830609
Mason, G. M., Li, G., Cohen, C. M. S., et al. 2012, ApJ, 761, 104
Montag, P., Egedal, J., Lichko, E., & Wetherton, B. 2017, PhPl, 24, 062906
Nalewajko, K., Uzdensky, D. A., Cerutti, B., Werner, G. R., & Begelman, M. C. 2015, ApJ, 815, 101
Oka, M., Birn, J., Battaglia, M., et al. 2018, SSRv, 214, 82
Oka, M., Ishikawa, S., Saint-Hilaire, P., Krucker, S., & Lin, R. P. 2013, ApJ, 764, 6
Oka, M., Krucker, S., Hudson, H. S., & Saint-Hilaire, P. 2015, ApJ, 799, 129
Oka, M., Phan, T.-D., Krucker, S., Fujimoto, M., & Shinohara, I. 2010, ApJ, 714, 915
Onofri, M., Isliker, H., & Vlahos, L. 2006, PhRvL, 96, 151102
Parker, E. N. 1965, P&SS, 13, 9
Pei, C., Bieber, J. W., Burger, R. A., & Clem, J. 2010, JGRA, 115, A12107
Provornikova, E., Laming, J. M., & Lukin, V. S. 2016, ApJ, 825, 55
Qiu, J., Liu, W., Hill, N., & Kazachenko, M. 2010, ApJ, 725, 319
Roytershteyn, V., Daughton, W., Karimabadi, H., & Mozer, F. S. 2012, PhRvL, 108, 185001
Shibata, K., & Tanuma, S. 2001, EP&S, 53, 473
Shih, A. Y., Lin, R. P., & Smith, D. M. 2009, ApJL, 698, L152
Stone, J. M., Gardiner, T. A., Teuben, P., Hawley, J. F., & Simon, J. B. 2008, ApJS, 178, 137
Strauss, R. D. T., & Effenberger, F. 2017, SSRv, 212, 151
Walker, J., Boldyrev, S., & Loureiro, N. 2018, PhRvE, 98, 033209
Wang, H., Lu, Q., Huang, C., & Wang, S. 2016, ApJ, 821, 84
Wang, L., Lin, R. P., Salem, C., et al. 2012, ApJL, 753, L23
Wang, L., Yang, L., He, J., et al. 2015, ApJL, 803, L2
Xu, Y., Fu, H. S., Liu, C. M., & Wang, T. Y. 2018, ApJ, 853, 11
Zank, G. P. (ed.) 2014, in Transport Processes in Space Physics and Astrophysics, Vol. 877 (Berlin: Springer), 185
Zank, G. P., le Roux, J. A., Webb, G. M., Dosch, A., & Khabarova, O. 2014, ApJ, 797, 28
Zhang, M. 1999, ApJ, 513, 409
Zhang, M., Jokipii, J. R., & McKibben, R. B. 2003, ApJ, 595, 493
Zhou, X., Büchner, J., Bárta, M., Gan, W., & Liu, S. 2015, ApJ, 815, 6
Zhou, X., Büchner, J., Bárta, M., Gan, W., & Liu, S. 2016, ApJ, 827, 94
Zweibel, E. G., & Yamada, M. 2009, ARA&A, 47, 291